ARTICLES
https://doi.org/10.1038/s41928-021-00573-1

nature electronics

Anomalous resistive switching in memristors based on two-dimensional palladium diselenide using heterophase grain boundaries

Yesheng Li[1], Leyi Loh[2], Sifan Li[1], Li Chen[1], Bochang Li[1], Michel Bosman[2] and Kah-Wee Ang[1,3] ✉

The implementation of memristive synapses in neuromorphic computing is hindered by the limited reproducibility and high energy consumption of the switching behaviour of the devices. Typical filament-type memristors suffer, in particular, from temporal and spatial variation in the set voltage and resistance states due to stochastic filament formation. Here, we report memristors based on two-dimensional pentagonal palladium diselenide ($PdSe_2$) that can exhibit anomalous resistive switching behaviour with two interchangeable reset modes: total reset and quasi-reset. Heterophase grain boundaries are formed in the $PdSe_2$ via local phase transitions induced by electron-beam irradiation, which leads to residual filaments along the grain boundaries that can guide the formation of conductive filaments. When operated in the quasi-reset mode, the memristors show a sixfold improvement in switching variation compared with devices operating in the total-reset mode, as well as a low set voltage (0.6 V), long retention times and programmable multilevel resistance states. We also show that the devices can emulate synaptic plasticity and that multipattern memorization can be implemented using a crossbar array architecture.

Memristive switching devices could be used to develop next-generation digital memory and neuromorphic computing due to their valuable properties including non-volatility, fast switching speeds and high endurance[1,2]. However, in the common metal–insulator–metal memristor, which is based on a filamentary switching mechanism, the operating voltage and resistance states suffer from undesirable temporal and spatial variations due to the random formation and rupture of conductive filaments[3–5]. Attempts have been made to improve the switching uniformity in memristors based on transition metal oxide by confining the formation of the filaments via an insertion layer[5,6], dislocations[7] and graphene nanopores[4,8,9]. However, these approaches still require an electroforming process, and suffer from low integration density and lack of flexibility.

Memristors based on two-dimensional (2D) materials are a promising alternative due to the fact that they are intrinsically thin and flexible, and could deliver reliable switching performance and scalability for practical neuromorphic computing applications[3,10]. Typically, resistive switching (RS) in 2D materials is the result of ion migration through the grain boundaries[11–18]. These grain boundaries are formed by the misorientation of grains (homophase grain boundaries) that contain abundant defects and favour the formation of conductive filaments[19,20]. Unfortunately, due to the stochastic forming process in homophase grain boundaries, memristors based on 2D materials suffer from uncontrollable ion transport through the boundaries, resulting in non-uniform and inconsistent RS[3,15–18]. Poor cycle-to-cycle and device-to-device variation would reduce online learning accuracy and hinders implementation in neuromorphic systems[1,21]. Therefore, the development of strategies to reliably control the formation of filaments is necessary for the practical use of memristors based on 2D materials.

In this Article, we report palladium diselenide ($PdSe_2$) memristors that have a switching mechanism driven by heterophase grain boundaries. Local phase transitions in $PdSe_2$ induced by electron-beam (e-beam) irradiation form heterophase grain boundaries with empty interface states and traps, which give rise to an interchangeable total/quasi-reset switching phenomenon that is not present in memristors based on homophase grain boundaries or transition metal oxides. Compared with memristors in the total-reset mode, memristors in the quasi-reset mode exhibit higher switching uniformity, reduced operating voltage, longer retention and reproducible multilevel RS. They also exhibit a sixfold improvement in switching uniformity that is achieved at a low set voltage. The behaviour is attributed to residual filaments along the heterophase grain boundaries guiding the formation of conductive filaments in the restricted region. Using such device structures, both short-term plasticity (STPL) and long-term plasticity (LTPL) characteristics are successfully emulated and multipattern memorization is implemented using a crossbar array architecture.

Electron-beam-irradiated $PdSe_2$-based memristor

Two-terminal cross-point RS devices, known as memristors, are proposed[22] as passive circuit elements that possess many unique circuit properties. Figure 1a shows a schematic illustration of a 5×5 crossbar array with an embedded memristor component in a vertical configuration (Fig. 1b). A corresponding cross-sectional transmission electron microscopy (TEM) image of the $PdSe_2$ memristor and an optical image of an experimentally realized crossbar array are shown in Fig. 1c,d, respectively. The memristor is configured in a vertical Ti/$PdSe_2$/Au structure, in which a $PdSe_2$ nanosheet (~3 nm) is used as the RS medium, and Ti and Au are used as the top active and bottom inert electrodes, respectively. The energy dispersive X-ray spectroscopy in Supplementary Fig. 1 further confirms the memristor structure.

Figure 1e plots the current–voltage (I–V) switching curves of memristors that undergo irradiation with different e-beam dosages.

[1]Department of Electrical and Computer Engineering, National University of Singapore, Singapore, Singapore. [2]Department of Materials Science and Engineering, National University of Singapore, Singapore, Singapore. [3]Institute of Materials Research and Engineering, A*STAR, Singapore, Singapore. ✉e-mail: eleakw@nus.edu.sg

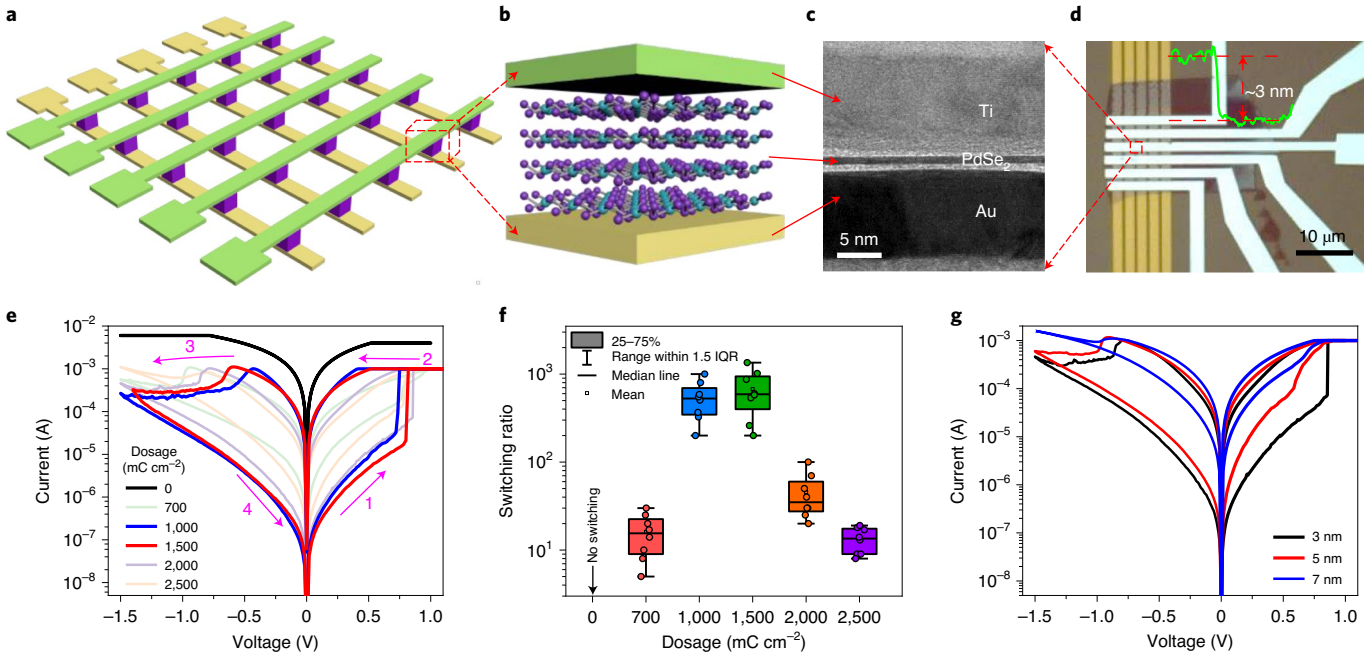

Fig. 1 | Ti/e-beam-irradiated $PdSe_2$/Au memristor. a, Schematic of the Ti/e-beam-irradiated $PdSe_2$/Au memristor in a 5 × 5 crossbar array architecture. **b**, Schematic of a single memristor in a vertical configuration. **c**, Cross-sectional TEM image showing the Ti/e-beam-irradiated $PdSe_2$/Au memristor. **d**, Optical image of a 5 × 6 memristive crossbar array architecture (the default size of the memristor is 2 μm × 2 μm). The inset is the height profile of the $PdSe_2$ nanosheet measured by atomic force microscopy. **e**, RS behaviours of the $PdSe_2$ memristors with different e-beam dosages. **f**, Dependence of switching ratio distribution on e-beam dosage (calculated from eight devices for each dosage). IQR, interquartile range. **g**, RS characteristics of the e-beam-irradiated memristors with different $PdSe_2$ thicknesses. For all *I*–*V* measurements, the Ti electrode is used as the top electrode to apply bias voltage and the Au electrode is used as the bottom electrode and grounded.

Without irradiation, the memristor shows no RS phenomenon. However, all e-beam-irradiated memristors exhibit forming-free bipolar non-volatile RS behaviour with a switching ratio up to 10^3, in which the optimal range of e-beam dosage is 1,000–1,500 mC cm^{-2} (Fig. 1f). Besides, a thinner e-beam-irradiated $PdSe_2$ nanosheet is shown to enable a higher switching ratio (Fig. 1g). By downscaling the $PdSe_2$ thickness to ~3 nm, the devices yield good uniformity for set voltage (V_{set}) and high-/low-resistance state (HRS/LRS) resistance (Supplementary Fig. 2). Moreover, the uniform bipolar RS behaviour can also be observed when the device size is scaled down to 100 nm × 100 nm (Supplementary Fig. 3).

Heterophase grain boundary formation via e-beam irradiation

$PdSe_2$ is a newly discovered pentagonal polymorphic transition metal dichalcogenide with an uncommon slightly asymmetrical layered network[23]. In its pristine form, $PdSe_2$ nanosheets show perfect lattice fringes (Fig. 2a,b) with a lattice spacing of 0.387 nm and 0.286 nm corresponding to (002) and (200) crystal planes of orthorhombic $PdSe_2$, respectively. When subject to e-beam irradiation, the $PdSe_2$ experiences distortion with apparent lattice disorders as marked by the yellow arrows, suggesting defect generation (Fig. 2c). Such defective structure is reproducible in other devices that undergo the same e-beam irradiation (Supplementary Fig. 4). Scanning transmission electron microscopy–annular dark field (STEM-ADF) with atomic resolution is employed to study the defective structure (Fig. 2d and Supplementary Fig. 5). A low acceleration voltage and a mild electron dose are used during the imaging to avoid introducing detrimental effects into the crystal structure. It can be confirmed that only lattice fringes of $PdSe_2$ are observed in the pristine sample (Fig. 2b). After e-beam irradiation, a region (region 1) with different lattice fringes from $PdSe_2$ (region 2) is observed in Fig. 2d, implying the formation of a new phase. The fast Fourier transform (FFT) of the whole region (Fig. 2e) shows a set of square diffraction patterns, suggesting an epitaxial relationship between the new phase and $PdSe_2$. However, the FFT pattern of region 1 (Fig. 2f) shows a dominant diffraction spot of (110) which is different from that of $PdSe_2$ (Fig. 2g), further confirming the presence of a new phase with a different lattice symmetry. The variation of the FFT patterns is consistent with the phase transformation from $PdSe_2$ to Pd_2Se_3 (ref. [24]). Such phase transition can be further verified by the X-ray photoelectron spectroscopy (Fig. 2i,j and Supplementary Fig. 6). For pristine $PdSe_2$, the two peaks at 336.94 eV and 342.20 eV (Fig. 2i) are ascribed to Pd $3d_{3/2}$ and Pd $3d_{5/2}$, respectively, whereas two other peaks at 54.95 eV and 55.78 eV (Supplementary Fig. 6a) are attributed to Se $3d_{3/2}$ and Se $3d_{5/2}$, respectively[25]. The appearance of a pair of new peaks (at 335.70 eV and 340.89 eV in Fig. 2j and 53.69 eV and 55.43 eV in Supplementary Fig. 6b) after irradiation implies the formation of a new phase. Therefore, the local phase transition is achieved under e-beam irradiation, resulting in the formation of heterophase grain boundaries. Due to the presence of different phases, a phase junction/potential barrier along with empty interface states (Fig. 2h)[26], which deviates from the common homophase grain boundaries, could be formed.

The fact that the non-irradiated memristors exhibit no RS phenomenon (Supplementary Fig. 7) indicates that the heterophase grain boundaries as generated by phase transition are responsible for the RS behaviour. To further study the RS mechanism as induced by heterophase grain boundaries, we employ conductive atomic force microscopy to record the current map (Supplementary Fig. 8), which clearly shows the formation of conductive filaments across the irradiated $PdSe_2$ nanosheet. However, when replacing Ti with

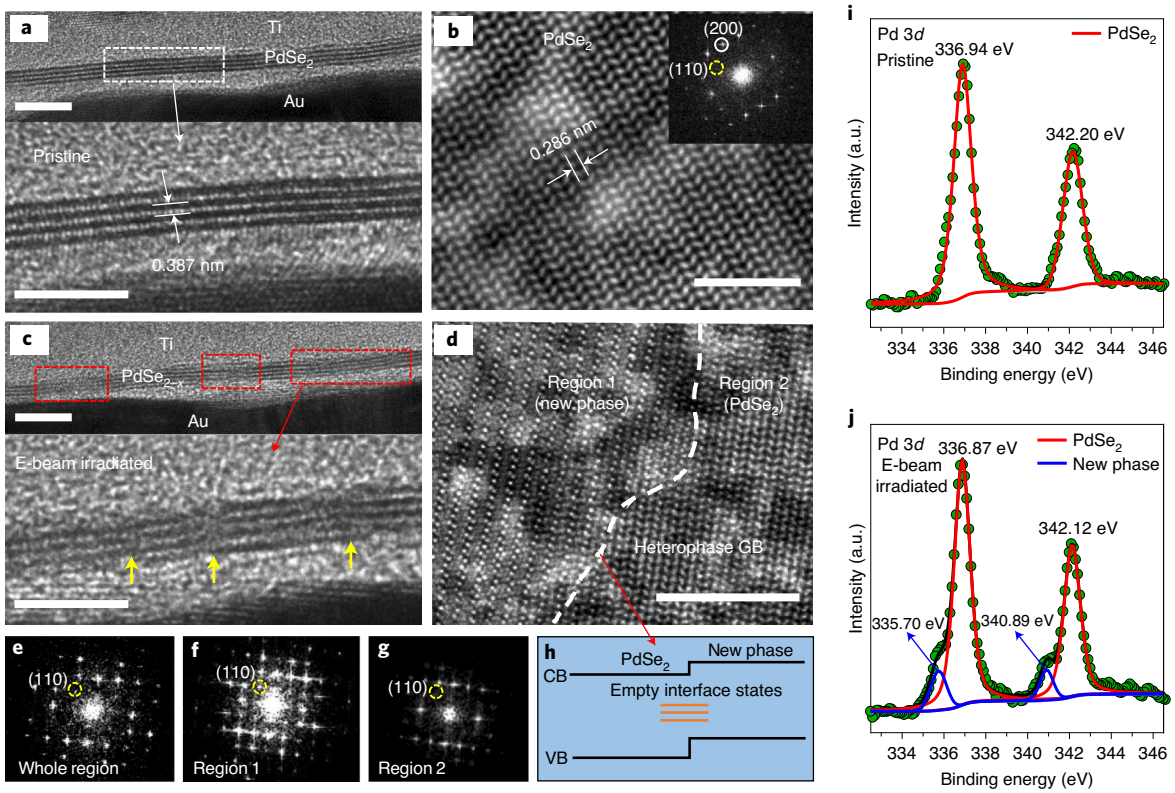

Fig. 2 | Heterophase grain boundary formation by e-beam irradiation. a–**d**, Cross-sectional high-resolution TEM images (**a**,**c**) and atomic-resolution top-view STEM-ADF images (**b**,**d**) of the pristine (**a**,**b**) and e-beam-irradiated (**c**,**d**) $PdSe_2$ (the red rectangular boxes correspond to distorted regions, and the yellow arrows in the zoomed-in image correspond to lattice disorder). GB, grain boundary. **e**–**g**, The corresponding FFT patterns of the whole region (**e**), region 1 (**f**) and region 2 (**g**). The FFT pattern of the pristine $PdSe_2$ is shown in the inset of **b**. **h**, Energy band diagram showing the formation of the heterophase junction/barrier with the unoccupied interface states in the heterophase grain boundaries. CB, conduction band; VB, valence band. **i**,**j**, X-ray photoelectron spectra of Pd 3*d* before (**i**) and after (**j**) e-beam irradiation. a.u., arbitrary units. The scale bars in **a**–**d** are 5 nm.

Pd as the top electrode (Supplementary Fig. 9), no RS behaviour can be observed, indicating that the migration of Ti active ions through the heterophase grain boundaries (that is, an electrochemical metallization mechanism, ECM) in the e-beam-irradiated $PdSe_2$ layer is contributing to the formation of conductive filaments. This can be confirmed by energy dispersive X-ray spectroscopy, in which an obvious Ti migration is observed after the memristor is switched on (Supplementary Fig. 10).

Anomalous RS with heterophase grain boundaries

To further explore the RS behaviour via the heterophase grain boundaries, continuous *I*–*V* measurements are performed using the memristor, which undergoes an e-beam irradiation of 1,500 mC cm^{-2}. The device is first preset to the LRS and then tested continually from Fig. 3a to Fig. 3h. As shown in Fig. 3a, there is no noticeable difference between the initial cycle and the subsequent sweep cycles, indicating that the device is electroforming free. When initially reset at −2 V (Fig. 3a), a two-step reset process is observed: first reset with a gradual current decrease, and second reset with an abrupt current drop. This causes a large V_{set} range of 1.85–2.58 V and an undesirable ΔV_{set} of 0.73 V. Even when the device is continually reset at a lower voltage of −1.5 V, a similar two-step reset and random set behaviour with V_{set} ranging from 1.64 to 2.29 V is observed, as shown in Fig. 3b. However, when the device experiences a low-voltage reset process at −1 V (Fig. 3c), a gentle one-step reset process is achieved for the same reset voltage of −1.5 V, showing a markedly reduced V_{set} of ~0.8 V and a tighter distribution of 0.19 V (Fig. 3d). Interestingly, when subsequently reset at −2 V, the *I*–*V* curves in Fig. 3e, which exhibit one-step reset process and narrow V_{set} distribution, also deviate from the behaviour shown in Fig. 3a. The different switching behaviours observed at the same reset voltage indicate the existence of two reset modes in our memristor, that is total reset and quasi-reset. The former shows a two-step reset process ending with an abrupt current spike, resulting in a complete rupture and random formation of filaments. The latter displays a gentle one-step reset process with a low and narrow distribution of V_{set}. Importantly, through a low-voltage reset process, the total-reset mode can be transformed into quasi-reset mode, as Fig. 3b is transformed to Fig. 3d via Fig. 3c.

In a similar fashion, the quasi-reset can also be transformed into the total-reset mode via a reset process with a high voltage (−2.5 V), as shown in Fig. 3f. Meanwhile, a uniform one-step reset process, that is quasi-reset mode, would reappear at −1.5 V (Fig. 3h) via a similar low-voltage reset process at −1.3 V (Fig. 3g). These findings indicate that the transformation between total-reset and quasi-reset modes can be achieved at a critical voltage (either −1.5 V or −2 V), which is interchangeable and reproducible, in the same device. Operating the memristor in quasi-reset mode at the critical voltage would maximize the device performance, including superior switching uniformity, low switching voltage and high switching ratio. It is worth noting that the quasi-reset mode is different from the common gradual reset, which lacks the interchangeable property (Supplementary Table 1).

Apparently, the anomalous RS is not observed in other ECM-based memristors using transition metal oxides or 2D materials with homophase grain boundaries, in which the switching curves usually display a one-step 'abrupt' reset process and absence of interchangeable property (Supplementary

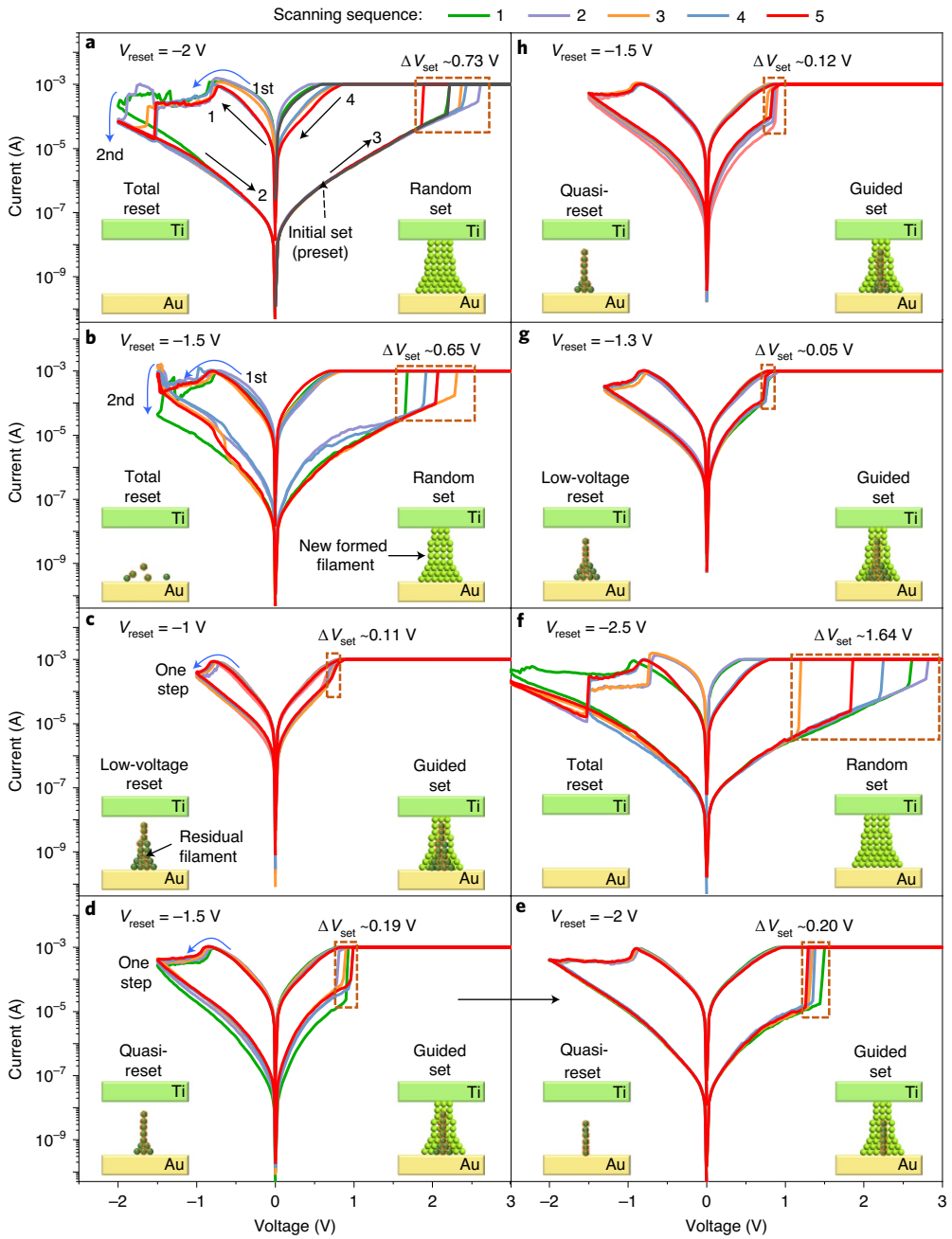

Fig. 3 | Interchangeable reset mode in the e-beam-irradiated $PdSe_2$ memristor. a–**h**, The memristor fabricated with e-beam dosage of 1,500 mC cm^{-2} is preset to the LRS and then measured continually from **a** to **h**. **a**, Reset at −2 V, a two-step reset process with a wide set voltage distribution of 1.85–2.58 V. **b**, Reset at −1.5 V, a two-step reset process with a large set voltage range of 1.64–2.29 V. **c**, Reset at −1 V, a one-step reset process with a tight set voltage range of 0.60–0.71 V. **d**, Reset at −1.5 V, a one-step reset process with a small set voltage change from 0.75 to 0.94 V. **e**, Reset at −2 V, a one-step reset process with a tight set voltage range of 1.25–1.45 V. **f**, Reset at −2.5 V, a two-step reset process with a wide set voltage range of 1.14–2.78 V. **g**, Reset at −1.3 V, a one-step reset process with set voltage range of 0.69–0.74 V. **h**, Reset at −1.5 V, a one-step reset process with set voltage range of 0.75–0.87 V. The value of ΔV_{set} is calculated as the maximum set voltage minus the minimum set voltage. Besides *I*–*V* curves, the corresponding filament evolutions are also shown in the insets.

Table 2)[13,18,27–29]. The anomaly may be attributed to the formation of heterophase grain boundaries with defective interfaces, which could contain heterojunctions with interface states that are usually absent from homophase grain boundaries[26]. This provides the conductive pathway for the memristive switching via the ECM process. Preliminary results also indicate that the HRSs in both modes could follow the space-charge-limited conduction mechanism, meaning that a charge trapping and detrapping process may be involved in the switching in addition to ECM[30] (Supplementary Fig. 11). However, the discrepancies from Child's law for HRS and the deviation from linearity for LRS imply that other conduction mechanisms may be present apart from space-charge-limited conduction. As such, a more thorough charge transport simulation would be needed to further investigate the underlying physics in the future, which is beyond the scope of the present work.

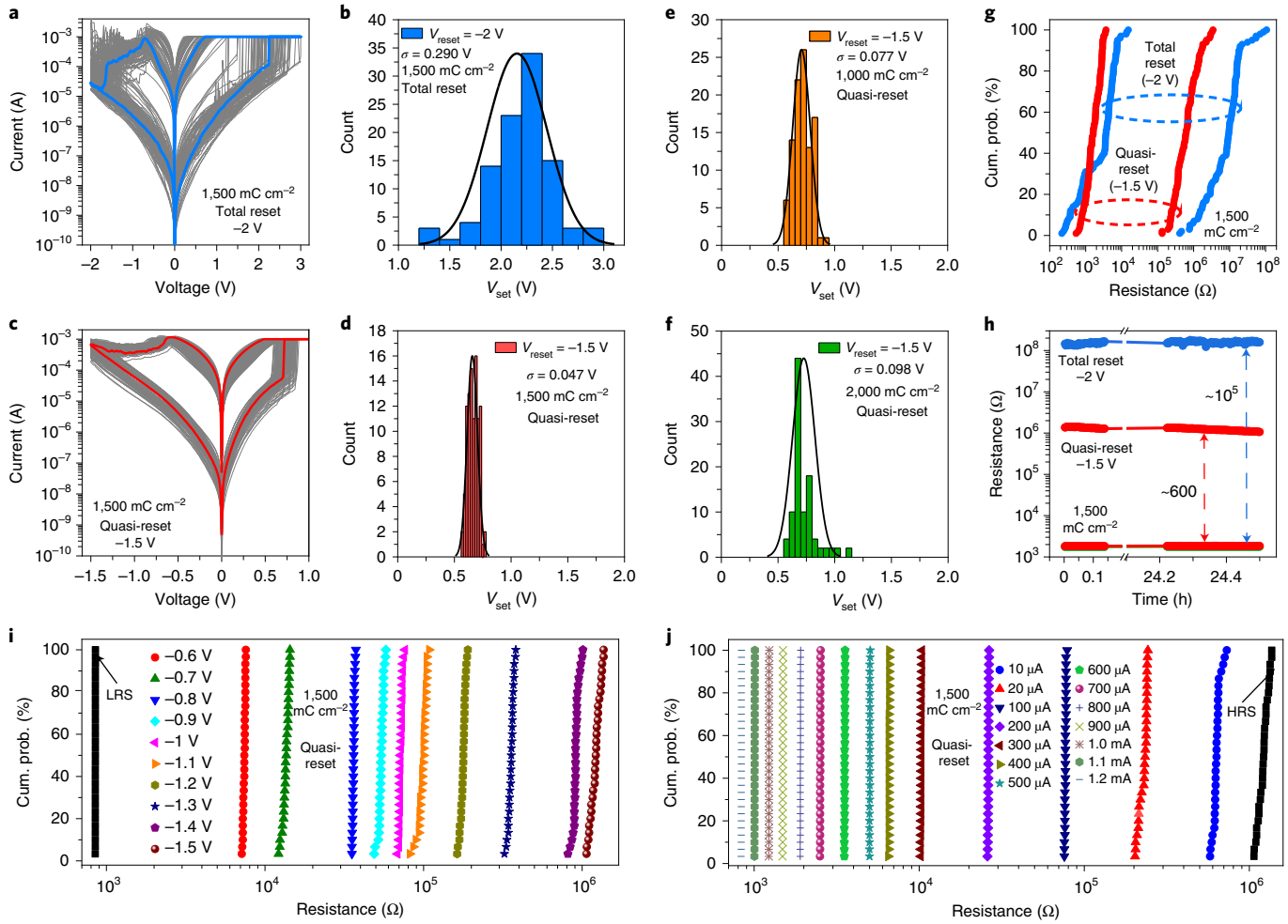

Fig. 4 | Reliable and multilevel RS in quasi-reset mode. a,**b**, *I*–*V* curves during 100 cycles (**a**) and the corresponding histogram of the set voltage (**b**) for a $PdSe_2$ memristor operating in total-reset mode. **c**,**d**, *I*–*V* curves during 100 cycles (**c**) and corresponding histogram of the set voltage (**d**) for a $PdSe_2$ memristor operating in quasi-reset mode. **e**,**f**, Histograms comparing the set voltage of $PdSe_2$ memristors in quasi-reset mode for e-beam irradiation dosages of 1,000 mC cm^{-2} (**e**) and 2,000 mC cm^{-2} (**f**) (calculated from *I*–*V* curves with 100 cycles, as shown in Supplementary Fig. 14). **g**, Cumulative probability plots of dynamic resistance for a $PdSe_2$ memristor with 1,500 mC cm^{-2} e-beam irradiation in quasi-reset mode (calculated from **a** and **c**). **h**, Retention results of the e-beam-irradiated $PdSe_2$ memristor (1,500 mC cm^{-2}) in total- and quasi-reset modes. **i**, Multiple HRSs recorded using different reset voltages for the $PdSe_2$ memristor in quasi-reset mode. **j**, Multiple LRSs recorded with varied compliance currents for the $PdSe_2$ memristor (1,500 mC cm^{-2}) in quasi-reset mode. All the resistances in **g**–**i** are read at 0.1 V.

Reliable and multilevel switching in quasi-reset mode

Cyclic electrical measurements are performed to further investigate the RS behaviour of the e-beam-irradiated $PdSe_2$ memristors that operate in different reset modes. The cyclic *I*–*V* curves of the memristor in total-reset mode show a bipolar switching behaviour with a two-step reset process (Fig. 4a). The V_{set} histogram shows a wide distribution ranging from 1.2 to 3 V, which is attributed to the random formation of the Ti filament. In contrast, when operating in quasi-reset mode, the reproducibility and repeatability of V_{set} are remarkably improved (Fig. 4c,d). A tighter V_{set} distribution of 0.6–0.9 V confirms the achievement of uniform switching. A quantitative analysis of the V_{set} s.d. (σ) shows a value of 0.290 V and 0.047 V for total reset and quasi-reset, respectively. This implies a sixfold reduction in set voltage variation, showing a substantially improved switching uniformity. Similarly, a tighter distribution of V_{set} is also demonstrated in memristors that are irradiated with 1,000 and 2,000 mC cm^{-2} (Fig. 4e,f). In addition, the variation in both HRS and LRS resistance dynamic ranges is reduced in quasi-reset mode (Fig. 4g). Nonetheless, regardless of the operating mode, the memristors exhibit superior retention performance, which could be maintained for longer than 10^5 s at room temperature without obvious degradation (Fig. 4h). Besides, the RS behaviour remains intact even after being stored in an ambient environment for a month, exhibiting superior environmental stability (Supplementary Fig. 15). Such negligible changes to conductance states with time and/or environment are critical to ensuring computing reliability. Additionally, more than 10 discrete HRSs and 14 discrete LRSs with small fluctuations are obtained when operating in quasi-reset mode by using different reset voltages and compliance currents, respectively (Fig. 4i,j and Supplementary Fig. 16a). Multiple resistance states are desirable for realizing the synaptic devices needed to build artificial neural networks. A performance benchmarking shows that the e-beam-irradiated $PdSe_2$ memristor achieves one of the best comprehensive performances, with a low V_{set} and competitive switching ratio, demonstrating the advantages over state-of-the-art non-volatile memristors based on other 2D materials (Supplementary Fig. 16b).

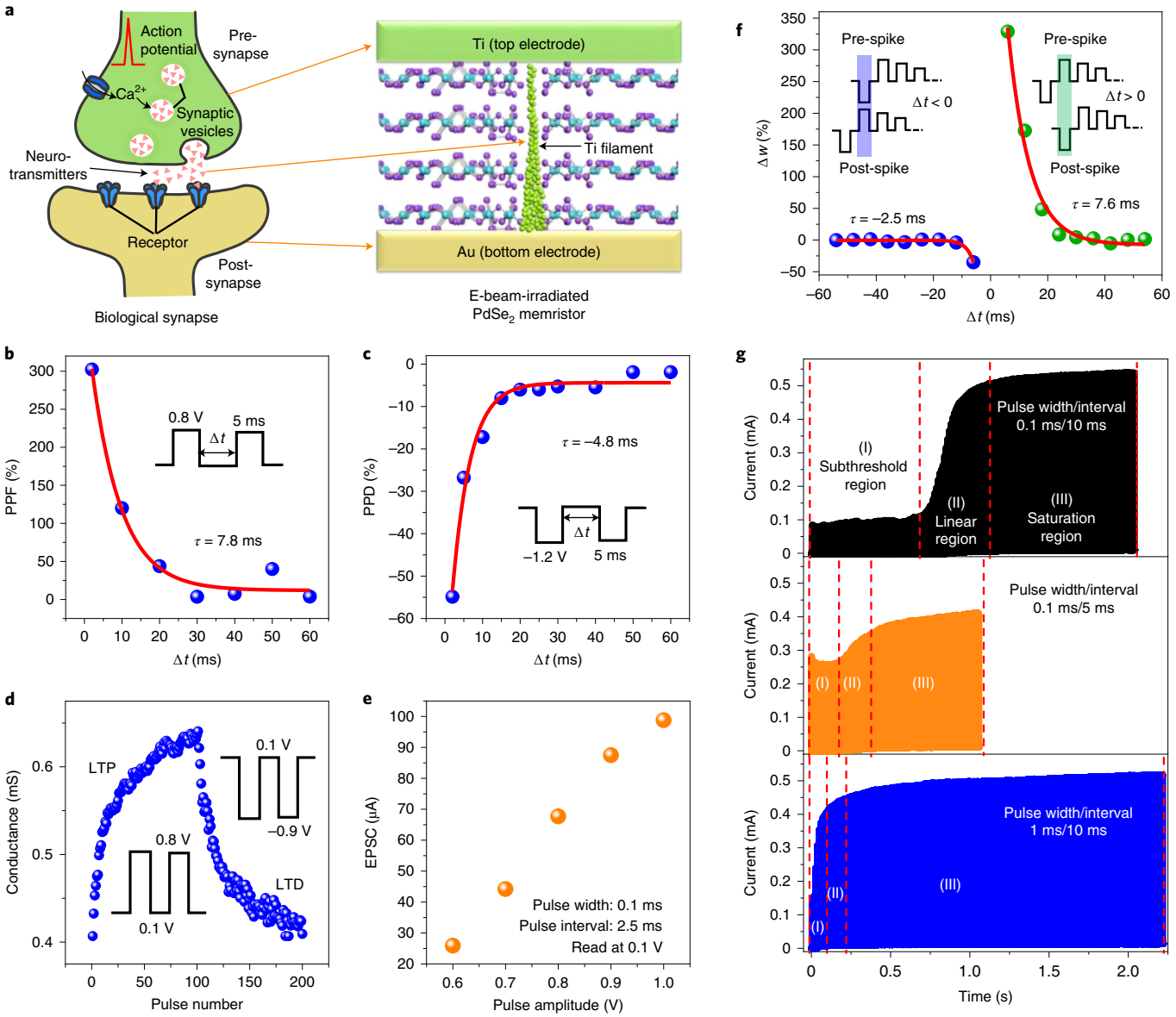

Fig. 5 | E-beam-irradiated $PdSe_2$ memristor in the quasi-reset mode for neuromorphic computing. a, Schematic showing the similarity between the structure of a biological synapse and the e-beam-irradiated $PdSe_2$ memristor. **b**,**c**, Δt-dependent PPF (**b**) and PPD (**c**), showing the STPL. The emulation of PPF and PPD is implemented by applying a pair of positive pulses and negative pulses, respectively. The PPF and PPD indexes are calculated from the expression $(A_2 - A_1)/A_1 \times 100\%$, where A_1 and A_2 are the peak amplitudes of the first and second responses, respectively. **d**, PSC versus pulse number, manifesting LTP and LTD processes (pulse width/interval: 0.1 ms/2.5 ms). **e**, Spike-amplitude-dependent plasticity of the synaptic memristor. **f**, Spike-timing-dependent plasticity of the synaptic memristor employing the pulse schemes in Supplementary Fig. 19a. For $\Delta t > 0$ and $\Delta t < 0$, the pulse train amplitudes of the pre- and post-spikes are −0.5, 0.5, 0.4, 0.35, 0.3, 0.25, 0.2, 0.15 and 0.1 V; Δw is defined as $\Delta w = (G_t - G_0)/G_0$, where G_t and G_0 are the conductances before and after overlapping spikes, respectively. **g**, Dynamic response of the synaptic memristor; the potentiation process can be controlled using pulse width and interval (the amplitudes are all fixed at 0.8 V). The red lines in **b**, **c** and **f** show the exponential fitting results using the equation $y = C_1 \exp(-x/\tau) + y_0$; the fitting time constant, τ, corresponds to the fast- and slow-decaying terms.

$PdSe_2$ memristor in quasi-reset mode for neuromorphic computing

The e-beam-irradiated $PdSe_2$ memristor emulates the structure and working principle of a biological synapse, in which the top and bottom electrodes mimic the presynapse and postsynapse, respectively (Fig. 5a). The most important characteristic of the biological synapse is synaptic plasticity, which includes STPL and LTPL[31]. Paired-pulse facilitation (PPF) and paired-pulse depression (PPD) are physiological phenomena associated with STPL, in which a previous stimulus enhances the subsequent synapse responses[32]. As indicated in Fig. 5b, the PPF index, which represents the temporal potentiation effect, is found to decrease with pulse interval, exhibiting an exponential decay function. Similarly, the PPD index (Fig. 5c), or the temporal depression effect, is also observed to exponentially decrease with pulse interval, showing short-term memory (STM).

The LTPL including long-term potentiation (LTP) and long-term depression (LTD) is emulated in Fig. 5d using positive and negative pulse sequences, respectively. Meanwhile, it also demonstrates the existence of a number of incremental accessible conductance

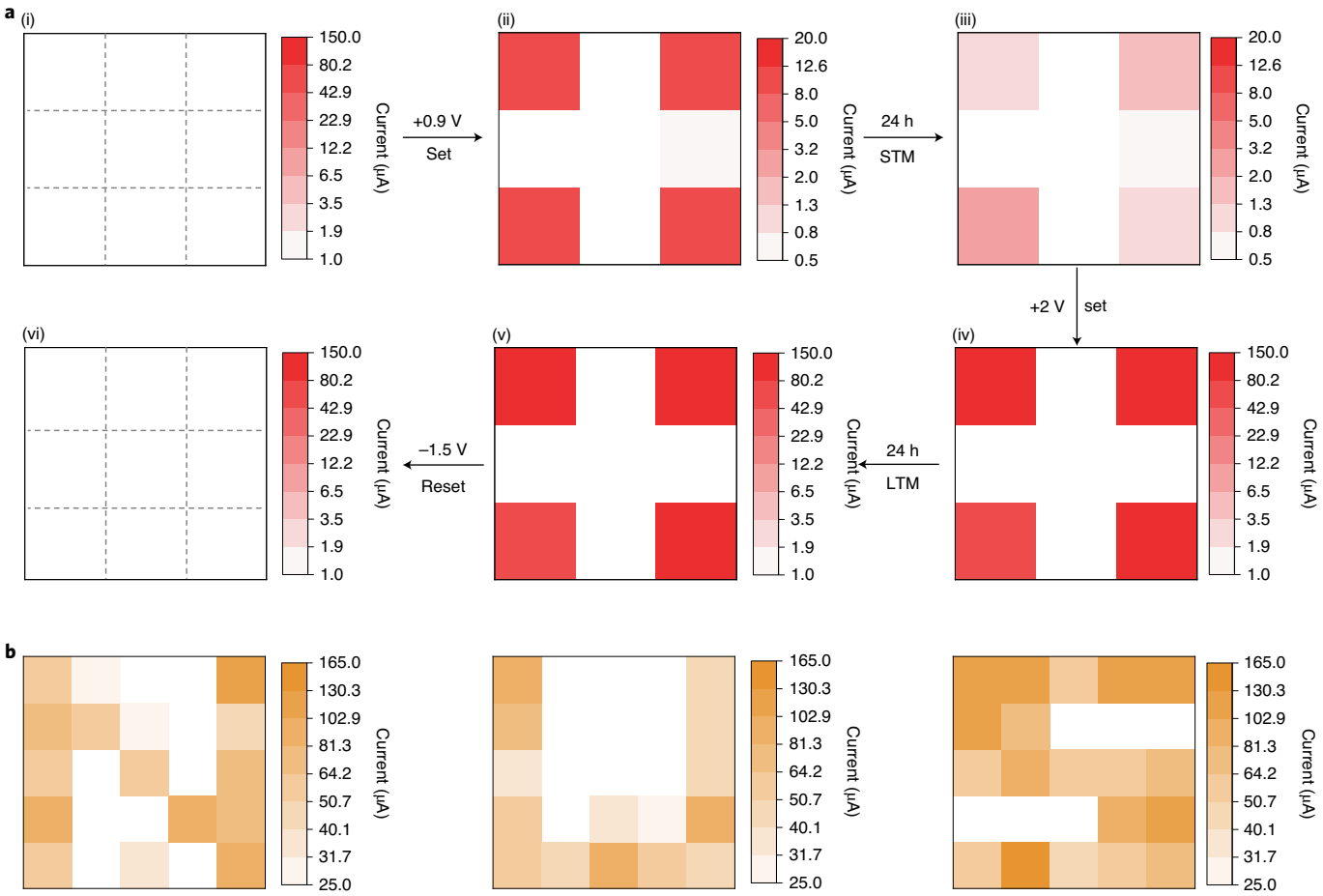

Fig. 6 | E-beam-irradiated $PdSe_2$ memristor in crossbar array architecture for pattern memorization. a, Dynamic process of STM and LTM in an e-beam-irradiated $PdSe_2$ memristive synaptic array. For the set process the pulse width, pulse interval and pulse number are 50 ns, 50 ns and 50, respectively, whereas for the reset process the pulse width, pulse interval and pulse number are 1 ms, 1 ms and 50, respectively. **b**, Memorization of a multipattern comprising 'N', 'U' and 'S' (single pulse, pulse width/amplitude: 5 ms/1 V). The colour level represents the current (read at 0.1 V). The operation details are shown in Supplementary Fig. 21.

states and reasonable linearity as well as symmetry, showing the potential for deep neural network application. Moreover, the LTP and LTD processes could be modulated by pulse amplitude, that is spike-amplitude-dependent plasticity, in which higher positive pulse amplitude causes an enhanced excitatory postsynaptic current (EPSC) and shortens time to reach saturated PSC (Fig. 5e and Supplementary Fig. 17a). In contrast, a higher negative pulse amplitude results in faster degradation of inhibitory PSC (Supplementary Fig. 17b,c). Similarly, the pulse width could also tune the LTPL, as a larger pulse width would result in an enhanced EPSC (Supplementary Fig. 17d). This indicates that the $PdSe_2$ memristor shows great plasticity in conductance tuning by adjusting the pulse parameter, manifesting the potential implementation of a deep neural network. Moreover, due to its low operating voltage, the device demonstrates an energy consumption of around 11 pJ per spike (Supplementary Fig. 18).

For LTPL, the synaptic plasticity is also dependent on the activities of pre- and postsynaptic neurons following the learning rules of spike-timing-dependent plasticity[32]. As shown in Fig. 5f, when the pre-spike precedes a post-spike with a short interval the synaptic weight (Δw) is enhanced, whereas when the post-spike precedes the pre-spike the Δw decreases. However, there is no change in Δw if the time interval between pre- and post-spikes is too large. The variation of Δw for both pulse interval $\Delta t > 0$ and $\Delta t < 0$ follows an exponential change, which is in good agreement with the response time of a biosynapse. The symmetry of spike-timing-dependent plasticity can be further improved by adjusting the voltage sequence (Supplementary Fig. 19b). The aforementioned results suggest that the e-beam-irradiated $PdSe_2$ memristor has the potential to be trained and achieve learning for spiking neural network application.

The dynamic EPSC characteristics can be studied by applying pulse sequences with different pulse widths and intervals. As illustrated in Fig. 5g, the EPSC curves can be divided into three regions: the subthreshold region (I), where the conductive filament is not formed, the linear region (II), where the conductive filament begins to form, resulting in a linear potentiation process, and the saturation region (III), where the conductive filament becomes stable and the PSC reaches saturation. It is found that either a shorter pulse interval or larger pulse width could narrow the transition from the subthreshold to the linear region, and shorten the time to reach the saturation region, indicating good plasticity with pulse programming. We show that the device working in quasi-reset mode can successfully mimic neuromorphic activities of the biological synapse and show better synaptic plasticity than that working in total-reset mode (Supplementary Fig. 20).

Dynamic process of short- and long-term memories

Human memory can be described as STM and long-term memory (LTM)[33]. To mimic the STM and LTM, four devices at the corners of a 3×3 memristor crossbar array are programmed by applying

50 voltage pulses with pulse width and interval fixed at 50 ns and 50 ns for each training sequence, respectively (Fig. 6a). The uniform initial state of the memristor crossbar array is shown in Fig. 6a(i). When subjected to initial small pulses of +0.9 V, the four corner devices are in the LRS (Fig. 6a(ii)) but this is diminished after 24 h (Fig. 6a(iii)), exhibiting the STM effect. However, when larger pulses of +2 V are applied, the current of the four devices is clearly retained after 24 h (Fig. 6a(iv),(v)), demonstrating the dynamic transition to LTM. Finally, the crossbar array can return to its initial state on applying negative pulses of −1.5 V (Fig. 6a(vi)). In short, the experiment successfully demonstrates the coexistence of STM and LTM in our $PdSe_2$ memristors with heterophase grain boundaries. Building on this capability, a memristive crossbar array architecture is designed and experimentally realized for pattern memorization. As shown in Fig. 6b, a multipattern comprising 'N', 'U' and 'S' can be recognized in a 5×5 crossbar array, albeit experiencing sneak current, indicating the potential of the $PdSe_2$ memristor for both digital memory and neuromorphic computing applications. To minimize the crosstalk issue further, one could integrate the e-beam-irradiated $PdSe_2$ memristor with a selector or a transistor to effectively suppress the sneak current. Further details of the crossbar array operation are given in Supplementary Fig. 21.

Conclusions

We have reported $PdSe_2$ memristors that exhibit an interchangeable total/quasi-reset RS behaviour driven by heterophase grain boundaries. When operating in the quasi-reset mode, the memristors show improved switching uniformity compared with devices in the total-reset mode, as well as a low operating voltage, multilevel data storage and long retention times. The residual filaments along the heterophase grain boundaries serve to guide the formation of conductive filaments at a low set voltage with minimal variability, which is critical to reduce energy consumption and improve learning accuracy. Synaptic plasticity behaviours are also successfully emulated and deployed for multipattern memorization, opening a route to the development of high-density crossbar arrays for artificial neural networks that can emulate complex neuromorphic learning.

Methods

Device fabrication. First, a layer of Ti/Au (5 nm/20 nm, acting as a bottom electrode) was deposited onto a 90 nm silicon dioxide layer through an e-beam evaporator. Next, a mechanically exfoliated $PdSe_2$ nanosheet (the crystal was purchased from HQ Graphene) was transferred onto the bottom electrode. Then the entire $PdSe_2$ nanosheet was irradiated by an e-beam with different dosages. The fabrication was completed by depositing a Ti/Al (20 nm/80 nm) top electrode. The e-beam source was from electron-beam lithography (type JBX-6300FS, acceleration voltage 100 keV, beam current 5 nA), and the top and bottom electrodes were also patterned by the same electron-beam lithography equipment with the same conditions using poly (methyl methacrylate) as the photoresist and isopropyl alcohol/methyl isobutyl ketone (1:3) as the developer. Devices with sizes of 2 μm × 2 μm and 100 nm × 100 nm are fabricated. Unless otherwise stated, the default size of the devices is 2 μm × 2 μm.

Device measurement. *I*–*V* characteristics were measured in ambient conditions at room temperature using an Agilent 4155B semiconductor parameter analyser and a probe station. The pulse measurements were carried out using a Cascade probe station connected to a 4200-SCS Keithley semiconductor analyser. For all *I*–*V* measurements, the Ti electrode was used as the top electrode to apply bias voltage and the Au electrode was used as the bottom electrode and grounded.

Material characterization. Cross-sectional TEM, high-resolution TEM and energy dispersive X-ray spectroscopy were conducted in a Talos F200X transmission electron microscope. Before TEM characterization, thin lamellae were fabricated using a focused ion beam (FEI, Helios NanoLab). Meanwhile, both pristine and e-beam-irradiated $PdSe_2$ nanosheets were transferred onto the polyporous Si_3N_4 grid for STEM-ADF analysis. Atomic-resolution STEM-ADF was performed on an aberration-corrected JEOL ARM200CFEG with a CEOS ASCOR STEM aberration corrector, operated at 80 kV acceleration voltage. The beam convergence semi-angle was set to 31 mrad with a collection detector angle ranging from 80 to 280 mrad, giving a probe size of around 0.1 nm. X-ray photoelectron spectroscopy characterizations were performed using a PHI Quantera II system with a monochromated Al anode. The source was operated at 15 kV with an emission current of 7 mA. The thickness of the $PdSe_2$ nanosheet was measured with a conductive atomic force microscope (Bruker Multimode V) working in contact mode using a platinum (Pt) tip with a radius of 25 nm and a spring constant of 3 N m^{-1}. The vertical memristor was constructed with an irradiated $PdSe_2$ nanosheet as the active switching layer, sandwiched by a Pt probe as the top electrode and Ti as the bottom electrode. The current map was collected under a constant bias of 100 mV after electrical stress.

Data availability

The data that support the plots within this article and other findings of this study are available from the corresponding author upon reasonable request.

Received: 25 April 2020; Accepted: 24 March 2021;
Published online: 17 May 2021

References

1. Xia, Q. & Yang, J. J. Memristive crossbar arrays for brain-inspired computing. *Nat. Mater.* **18**, 309–323 (2019).
2. Wang, C.-Y. et al. 2D layered materials for memristive and neuromorphic applications. *Adv. Electron. Mater.* **5**, 1901107 (2019).
3. Li, Y., Long, S., Liu, Q., Lv, H. & Liu, M. Resistive switching performance improvement via modulating nanoscale conductive filament, involving the application of two-dimensional layered materials. *Small* **13**, 1604306 (2017).
4. Zhao, X. et al. Confining cation injection to enhance CBRAM performance by nanopore graphene layer. *Small* **13**, 1603948 (2017).
5. Tsai, T. L., Jiang, F. S., Ho, C. H., Lin, C. H. & Tseng, T. Y. Enhanced properties in conductive-bridge resistive switching memory with oxide–nitride bilayer structure. *IEEE Electron Device Lett.* **37**, 1284–1287 (2016).
6. Kumar, D., Aluguri, R., Chand, U. & Tseng, T.-Y. Enhancement of resistive switching properties in nitride based CBRAM device by inserting an Al_2O_3 thin layer. *Appl. Phys. Lett.* **110**, 203102 (2017).
7. Choi, S. et al. SiGe epitaxial memory for neuromorphic computing with reproducible high performance based on engineered dislocations. *Nat. Mater.* **17**, 335–340 (2018).
8. Lee, J., Du, C., Sun, K., Kioupakis, E. & Lu, W. D. Tuning ionic transport in memristive devices by graphene with engineered nanopores. *ACS Nano* **10**, 3571–3579 (2016).
9. Zhao, X. L. et al. Breaking the current-retention dilemma in cation-based resistive switching devices utilizing graphene with controlled defects. *Adv. Mater.* **30**, 1705193 (2018).
10. Zhang, L., Gong, T., Wang, H. D., Guo, Z. N. & Zhang, H. Memristive devices based on emerging two-dimensional materials beyond graphene. *Nanoscale* **11**, 12413–12435 (2019).
11. Sangwan, V. K. et al. Multi-terminal memtransistors from polycrystalline monolayer molybdenum disulfide. *Nature* **554**, 500–504 (2018).
12. Wang, L. et al. Artificial synapses based on multiterminal memtransistors for neuromorphic application. *Adv. Funct. Mater.* **29**, 1901106 (2019).
13. Prakash, R., Sharma, S., Kumar, A. & Kaur, D. Improved resistive switching performance in Cu-cation migrated MoS_2 based ReRAM device incorporated with tungsten nitride bottom electrode. *Curr. Appl. Phys.* **19**, 260–265 (2019).
14. Feng, X. et al. A fully printed flexible MoS_2 memristive artificial synapse with femtojoule switching energy. *Adv. Electron. Mater.* **5**, 1900740 (2019).
15. Pan, C. B. et al. Coexistence of grain-boundaries-assisted bipolar and threshold resistive switching in multilayer hexagonal boron nitride. *Adv. Funct. Mater.* **27**, 1604811 (2017).
16. Hui, F. et al. Synthesis of large-area multilayer hexagonal boron nitride sheets on iron substrates and its use in resistive switching devices. *2D Mater.* **5**, 7 (2018).
17. Zhuang, P. et al. Nonpolar resistive switching of multilayer-hBN-based memories. *Adv. Electron. Mater.* **6**, 1900979 (2019).
18. Yan, X. et al. Robust Ag/ZrO_2/WS_2/Pt memristor for neuromorphic computing. *ACS Appl. Mater. Interfaces* **11**, 48029–48038 (2019).
19. Ly, T. H. et al. Misorientation-angle-dependent electrical transport across molybdenum disulfide grain boundaries. *Nat. Commun.* **7**, 10426 (2016).
20. Lanza, M. et al. Grain boundaries as preferential sites for resistive switching in the HfO_2 resistive random access memory structures. *Appl. Phys. Lett.* **100**, 123508 (2012).
21. Zhang, Y. et al. Brain-inspired computing with memristors: challenges in devices, circuits, and systems. *Appl. Phys. Rev.* **7**, 011308 (2020).
22. Chua, L. O. Memristor—the missing circuit element. *IEEE Trans. Circuit Theory* **18**, 507–519 (1971).
23. Oyedele, A. D. et al. $PdSe_2$: pentagonal two-dimensional layers with high air stability for electronics. *J. Am. Chem. Soc.* **139**, 14090–14097 (2017).
24. Lin, J. H. et al. Novel Pd_2Se_3 two-dimensional phase driven by interlayer fusion in layered $PdSe_2$. *Phys. Rev. Lett.* **119**, 016101 (2017).

25. Liang, F.-X. et al. Light confinement effect induced highly sensitive, self-driven near-infrared photodetector and image sensor based on multilayer $PdSe_2$/pyramid Si heterojunction. *Small* **15**, 1903831 (2019).
26. Zuluaga, S., Lin, J. H., Suenaga, K. & Pantelides, S. T. Two-dimensional $PdSe_2$–Pd_2Se_3 junctions can serve as nanowires. *2D Mater.* **5**, 035025 (2018).
27. Zhuge, F. et al. Improvement of resistive switching in Cu/ZnO/Pt sandwiches by weakening the randomicity of the formation/rupture of Cu filaments. *Nanotechnology* **22**, 275204 (2011).
28. Tsuruoka, T., Terabe, K., Hasegawa, T. & Aono, M. Forming and switching mechanisms of a cation-migration-based oxide resistive memory. *Nanotechnology* **21**, 425205 (2010).
29. Rehman, S. et al. Thickness-dependent resistive switching in black phosphorus CBRAM. *J. Mater. Chem. C* **7**, 725–732 (2019).
30. Zhu, J., Zhang, T., Yang, Y. & Huang, R. A comprehensive review on emerging artificial neuromorphic devices. *Appl. Phys. Rev.* **7**, 011312 (2020).
31. Nicholls, J. G., Martin, A. R., Wallace, B. G. & Fuchs, P. A. *From Neuron to Brain* 271 (Sinauer, 2001).
32. Yang, R., Huang, H.-M. & Guo, X. Memristive synapses and neurons for bioinspired computing. *Adv. Electron. Mater.* **5**, 1900287 (2019).
33. Kumar, M., Ban, D.-K., Kim, S. M., Kim, J. & Wong, C.-P. Vertically aligned WS_2 layers for high-performing memristors and artificial synapses. *Adv. Electron. Mater.* **5**, 1900467 (2019).

Acknowledgements

This work is supported by A*STAR Science and Engineering Research Council (no. A2083c0061), and by the National Research Foundation, Prime Minister's Office, Singapore, under its Competitive Research Programme (NRF-CRP24-2020-050). We thank A. V.-Y. Thean, Y. Li, X. Feng and X. Gong in the Department of Electrical and Computer Engineering, and K. P. Loh and L. Wang in the Department of Chemistry, National University of Singapore, for valuable help in device measurements.

Author contributions

This project was supervised and directed by K.-W.A. Y.L. and K.-W.A. conceived this work. Y.L. and K.-W.A. designed the experiments. Y.L., S.L. and B.L. performed the device fabrication. Y.L. and S.L. conducted the electrical measurements. Y.L. and L.C. performed the material characterization. L.L. and M.B. performed the STEM-ADF imaging. All authors contributed to the discussion and analysis of results. Y.L. and K.-W.A. wrote the manuscript.

Competing interests

The authors declare no competing interests.

Additional information

Supplementary information The online version contains supplementary material available at https://doi.org/10.1038/s41928-021-00573-1.

Correspondence and requests for materials should be addressed to K.-W.A.

Peer review information *Nature Electronics* thanks Shibing Long and the other, anonymous, reviewer(s) for their contribution to the peer review of this work.

Reprints and permissions information is available at www.nature.com/reprints.

Publisher's note Springer Nature remains neutral with regard to jurisdictional claims in published maps and institutional affiliations.